Gradient Phosphatized Interphase for Ultra-Stable and Low-Temperature Zinc Metal Batteries

Wei Wang
Nankai University
Shan Chen
Nankai University
Xuelong Liao
Nankai University
Rong Huang
Nankai University
Jialei Chen
Nankai University
Yaxin Wang
Nankai University
Fei Wang
Fudan University https://orcid.org/0000-0002-2057-5130
Huan Wang (Huan.wang0520@nankai.edu.cn)
Nankai University https://orcid.org/0000-0001-8419-8402

Article

Keywords: Zn metal anodes, Gradient phosphatized SEI, Low temperature, Rapid interfacial kinetics, Long-term stability, Aqueous Zn batteries

Posted Date: October 20th, 2022

DOI: https://doi.org/10.21203/rs.3.rs-2143664/v1

Version of Record: A version of this preprint was published at Nature Communications on September 6th, 2023. See the published version at https://doi.org/10.1038/s41467-023-41276-9.

Abstract

In situ formation of a stable solid electrolyte interphase (SEI) layer on zinc (Zn) surface is an effective solution to suppress dendrite growth. However, the fast transport of bivalent Zn-ions within the solid interlayer remains very challenging. Herein, we engineer the SEI components and enable a superior kinetic of Zn metal under harsh conditions. Trimethyl phosphate was employed as a cosolvent, which decreases the freezing point of water and spontaneously generate a gradient ZnF_2–$Zn_3(PO_4)_2$ interphase. Mechanistic studies reveal the outer ZnF_2 facilitates Zn^{2+} desolvation and inner $Zn_3(PO_4)_2$ serves as channels for Zn^{2+} transport, contributing to long-term cycling at subzero temperatures. Impressively, the gradient SEI enables a record lifespan of symmetric Zn cells over 6000 hours (~ 8 months) at − 50 °C. Furthermore, the Zn–KVOH full cell achieves a superhigh areal capacity (9.42 mAh cm^{-2}) under a practical cycling condition (high cathode loading: 33.75 mg cm^{-2}; lean electrolyte: 6.76 μL mAh^{-1}), and delivers a capacity retention of 86.1% after 12000 cycles at − 50 °C. This work provides a feasible route for low-temperature aqueous Zn metal batteries.

Introduction

The ever-increasing demand of renewable energy sources (such as solar and wind) and their fluctuating nature necessitate the development of grid-scale energy storage technologies to minimize the fossil fuel consumption. Aqueous zinc (Zn) metal batteries (ZMBs) have been prospected as appealing choices for enabling more economical and large-scale battery systems due to their abundant reserves, low manufacturing cost, high safety and intrinsic merits of Zn metal including high theoretical capacity (820 mAh g^{-1} and 5855 mAh mL^{-1}) and low redox potential (− 0.76 V versus the standard hydrogen electrode)[1–5]. However, in terms of the stationary energy storage applications in cold climates or high-latitude regions rich in renewable energy, the ZMBs suffer from severe performance degradation and even fail to work due to the solidification of the aqueous electrolyte and deteriorated electrode/electrolyte interphase at subzero temperatures[6–9].

The hydrogen (H)-bonds between water molecules become stronger as temperature drops, which drives the disordered water into ordered ice[10,11]. Thus, tuning the electrolyte compositions to break the intermolecular H-bonds in water has been regarded as a general principle to prevent water from solidifying. In this respect, the prevailing research focuses on the following three approaches: *i*) employing concentrated aqueous electrolyte that can provide abundant ions to bond with O–H in water[7,12–14]; *ii*) introducing additives/cosolvents to reform H-bonds with water[8,15–18]; *iii*) fabricating hydrogel composed of cross-linked hydrated polymer to intensify the interaction with water[19,20]. These strategies have enabled the water-based electrolyte with good low-temperature adaptability, but the cycling life of low-temperature Zn metal anode is generally limited to hundreds of hours, which is far from satisfactory for practical implementation.

The chemically instable nature of Zn metal against water causes the continuous and slow H_2 reaction at low temperatures. This can result in the local enhancement of OH^- concentration, which in turn corrodes the Zn metal surface through formation of loose and plate-like passivation film, leading to uncontrolled Zn dendrite growth and eventual cell failure[21–23]. In this scenario, building dense solid electrolyte interphase (SEI) that can block water penetration is the most effective route to suppress the parasitic reactions and ensure durable Zn metal anodes[2,12]. However, learning from the former experiences on low-temperature lithium (Li) batteries[24–26], the interface kinetics associated with Zn^{2+} desolvation and conduction are extremely sluggish at low temperatures, which are mainly responsible for the poor cycling performance. Compared with Li-ions, it is more challenging for the bivalent Zn-ions to cross the as-formed SEI at subzero temperatures, thus resulting in huge cell impedance, non-uniform deposition and severe capacity decay. Therefore, regulating the components and distribution of the as-formed SEI on Zn surface to lower the kinetic barrier of Zn^{2+} desolvation and its transport through the SEI is the key premise for achieving ultra-stable cycling behaviors under low-temperature condition, however, has rarely been explored.

The engineering of electrolyte chemistry can simultaneously mitigate the two issues of low-temperature ZMBs including water solidification and SEI-related kinetics, which is also the simplest approach that could be easily adapted to practical applications. Herein, trimethyl phosphate (TMP) was selected as a cosolvent into the aqueous electrolyte for safe and anti-freezing ZMBs in view of its high Gutmann donor number, fire retardance, low viscosity and miscibility with water[27–29]. With a volume ratio of 40%, TMP can greatly break the H-bonds in water through interacting with water that endows the hybrid electrolyte with a low freezing point of − 56.8 ^oC and a high ionic conductivity of 0.85 mS cm^{-1} at − 50°C. Both the experimental characterizations and calculation results reveal that the TMP addition can regulate the Zn^{2+} solvation structure to in situ form gradient SEI composed of outer ZnF_2 and inner $Zn_3(PO_4)_2$ (Fig. 1), which can promote the desolvation of Zn^{2+} on the interface and facilitate rapid transport across the SEI, respectively. As a result of the joint effects, it achieves an average Coulombic efficiency of 99.9% over 3800 cycles at − 30°C and remarkable durability over 6000 hours at − 50°C, which represent the best low-temperature ZMBs performance to the best of our knowledge. Furthermore, high-capacity full cells with KVOH as cathode were also demonstrated with superb capacity retention ability.

Results

Exploring optimal formulation for low-temperature aqueous electrolyte

A series of TMP/water hybrid electrolytes with 2 M zinc trifluoromethanesulfonate ($Zn(OTf)_2$) were prepared, where the volume percentage of TMP ranges from 0%, 5%, 10%, 20%, 40%, 60%, 80–100%, and the corresponding electrolyte is marked as TMP–0, TMP–5, TMP–10, TMP–20, TMP–40, TMP–60, TMP–80 and TMP–100, respectively. After 3 h of resting at − 50 ^oC, the TMP–40, TMP–60 and TMP–80

can maintain the liquid state without deposit or phase separation, whereas crystallization/solidification was observed in the other counterparts (Fig. 2a). Further, the differential scanning calorimeter (DSC) curves show the freezing points of the hybrid electrolytes are lowered to − 56.8°C as the TMP content reaches 40% (Fig. 2b and Supplementary Fig. 1), which can be explained by the breakage of H-bonds network in water molecules by TMP co-solvent. On the other hand, the ionic conductivity negatively correlates to the content of TMP in the temperature ranging from − 30 ^{o}C to 60 ^{o}C (Fig. 2c, Supplementary Fig. 2 and Supplementary Table 1), possibly due to a slight increase in electrolyte viscosity. However, the TMP–0 exhibits a sudden drop in ionic conductivity below − 30 ^{o}C, because of the high freezing point (− 34.8 ^{o}C in DSC) that causes the electrolyte solidification. In sharp contrast, the TMP–40 exhibits a slow decline in ionic conductivity as the temperature decreases and achieves a high ionic conductivity of 0.85 mS cm^{-1} even at − 50°C (> 0.1 mS cm^{-1})[26], several orders of magnitude higher than that of TMP–0.

To explore the molecular interaction within the hybrid electrolytes, a series of spectroscopic characterizations were performed. The Raman peaks associated with O–H stretching vibration of water molecules are visible within the range from 3100 to 3800 cm^{-1}, which can be divided into three peaks including strong, weak and non H-bonds (Fig. 2d, e, and Supplementary Figs. 3–4)[7,30]. It was found that the probability of non-H bonds increases with TMP content, while the change of strong-H bonds shows the opposite trend (Fig. 2f). Notably, as the TMP content was increased to 40%, the percentage of non H-bond almost reaches the maximum. Moreover, the Fourier transform infrared (FTIR) results in Supplementary Fig. 5 show that the O–H and C–H stretching vibration modes experience significant blueshifts and redshifts with the increase of TMP, respectively, largely ascribed to the breakage of H-bond in water along with the H-bond formation between TMP and water in the hybrid electrolyte[8]. This can be further confirmed by the ^{1}H nuclear magnetic resonance (NMR) spectra (Fig. 2g and Supplementary Fig. 6), wherein the ^{1}H from H_2O and TMP both chemical shift to low field with the increase of TMP. These results reveal that the TMP can interact with water to reform H-bonds, during which the H-bonds in water were largely destroyed, thus affording a low freezing point and high ionic conductivity of the hybrid electrolyte at low temperatures. To maximally inherit the unique merits of aqueous electrolyte, TMP–40 is considered as the optimal electrolyte formulation for low-temperature ZMBs. Also, the TMP–40 endows the separator with high fire retardance (Supplementary Fig. 7), indicating the hybrid electrolyte is safe enough to operate.

Solvation Structure And Sei Characterization

Since the SEI components highly depend on the solvation sheath of Zn^{2+}, we furthered the study of Zn^{2+} solvation structure in a series of TMP/H_2O electrolytes through theoretical calculations and experimental characterizations. The Raman characterizations shows the SO_3 stretching band in the OTf^{-}–anions experiences a gradual shift with the increase of TMP concentration (Fig. 3a and Supplementary Fig. 8). The broad peaks can be well fitted into three peaks at ~ 1028 cm^{-1}, ~ 1033 cm^{-1} and ~ 1040 cm^{-1}, corresponding to the free anion (FA, OTf^{-}), solvent-separated ion pairs (SSIP, Zn^{2+}–$(H_2O)_x(TMP)_y$–OTf^{-})

and contact ion pairs (CIP, Zn^{2+}–OTf^{-}), respectively[31,32], as shown in Supplementary Fig. 9. By calculating the peak area ratio, the CIP percentage increases with the increase of TMP concentration and reaches the maximum value of 51.92% with 40% of TMP (Supplementary Fig. 10), indicating OTf^{-} anion is involved in the Zn^{2+} solvation sheath. Afterwards, the CIP content decreases with the increase of TMP, possibly due to the strong binding of TMP and Zn^{2+} that causes more TMP to enter the Zn^{2+} solvation sheath by substituting partial OTf^{-} anions. Meanwhile, there is a V-shape relationship between FA percentage and TMP concentration, where the lowest FA ratio is 6.59%, suggestive of more OTf^{-} involved in the solvated structure of Zn^{2+}. This also confirms that TMP–40 is the optimized electrolyte formulation for in-situ formation of favorable SEI to suppress side reactions and facilitate Zn^{2+} transport. For the Raman spectra of the TMP, the P–O–(C) symmetric stretching vibration gradually blueshifts as the increase of TMP (Fig. 3b and Supplementary Fig. 11), indicating more TMP participates in the Zn^{2+} solvation shell[33,34], according well with the above results. This is also supported by the higher binding energy of Zn^{2+}–TMP complex (– 200.36 KJ mol^{-1}) compared with Zn^{2+}–H_2O complex (– 104.54 KJ mol^{-1}), as shown in Supplementary Fig. 12.

To ascertain the coordination number of anions and solvents in the solvation sheath of TMP–40, molecular dynamic (MD) simulations were carried out. The numbers of Zn^{2+}, OTf^{-}, TMP and H_2O in the hybrid electrolytes are summarized in Supplementary Table 2. As shown by the snapshots from the simulated solvation structure (Supplementary Figs. 13–14), some water molecules are squeezed out of the Zn^{2+} solvation shell in the TMP–40 electrolyte and partially replaced with TMP solvent and OTf^{-} anions. According to the radial distribution functions (RDF) in Fig. 3c, the Zn–O peak in OTf^{-}, TMP and H_2O correspond to the distance of 0.19, 0.25 and 0.23 nm, respectively, further validating that the OTf^{-}, TMP and H_2O molecules incorporate into the first solvation shell of Zn^{2+}. Accordingly, the respective coordination number was calculated to be 0.85, 0.14 and 5.01, constituting a CIP–type solvation shell of $Zn^{2+}[H_2O]_{5.01}[TMP]_{0.14}[OTf^{-}]_{0.85,}$ which favors the in-situ formation of SEI on Zn surface through reductive decomposition. Note that the small amount of TMP and OTf^{-} involved in the solvation shell is beneficial to form a thin SEI layer, which facilitates fast Zn^{2+} transfer. Moreover, the Zn^{2+} desolvation energy of TMP–0 and TMP–40 can be obtained by extracting the respective R_{ct} before cycling, where no SEI was formed on Zn surface. As shown in Supplementary Fig. 15, the addition of TMP causes a slight increase in the energy barrier for dissociation of Zn^{2+}, largely ascribed to the strong interaction of Zn^{2+}–TMP and Zn^{2+}–OTf^{-}, which in turn allows for the stepwise formation of ZnF_2–$Zn_3(PO_4)_2$.

With the TMP–40 as the optimal electrolyte formulation, the linear sweep voltammetry (LSV) measurements were first performed to examine the electrochemical stability. It was found that the TMP–40 electrolyte can effectively suppress the water decomposition over a wide electrochemical window and prevent Zn surface corrosion (Supplementary Figs. 16–17). Moreover, the disappearance of the cathodic peak at ~ 0.1 V accompanied with the decrease in current density after five cycles also indicates the SEI was formed at the initial plating and can inhibit the hydrogen evolution reaction (HER) (Supplementary

Fig. 18). After 40 cycles of stripping/plating of Zn metal, X-ray diffraction (XRD) peaks corresponding to the zinc triflate hydroxide hydrate ($Zn_xOTf_y(OH)_{2x-y}{\cdot}nH_2O$, ZOTH) were detected on the Zn surface in TMP−0 (Supplementary Fig. 19), which can largely restrict the transport of Zn^{2+} and lead to dendrite growth[31,35]. In contrast, no byproduct was observed in TMP−40. X-ray photoelectron spectroscopy (XPS) with Ar ion sputtering was further employed to determine the depth distribution of composition in SEI formed on Zn surface. As shown in Fig. 3d, the top SEI layer (before sputtering) is rich in $-CF_3$ species (~ 688.8 eV) and inorganic ZnF_2 (~ 684.1 eV) with a tiny amount of $Zn_3(PO_4)_2$ (~ 134.3 eV). Accordingly, the lattice fringes in the high-resolution transmission electron microscopy (HRTEM) corresponding to the planes of ZnF_2 and $Zn_3(PO_4)_2$ were clearly observed with uniform distribution (Fig. 3e, f and Supplementary Fig. 20), consistent with the XPS results. Based on the previous reports[28,31], the $-CF_3$ species arises from either the incomplete reduction of OTf^- or the residual salt on Zn surface, while ZnF_2 and $Zn_3(PO_4)_2$ are attributed to the decomposition product of $Zn^{2+}-OTf^-$ and $Zn^{2+}-TMP$ complexes. As the sputtering continues, the peak intensity of $Zn_3(PO_4)_2$ distinctly becomes stronger along with the decrease in ZnF_2 peak (Fig. 3d and Supplementary Fig. 21). After 310 s of sputtering, the $Zn_3(PO_4)_2$ gradually becomes the major composition in the SEI. In sharp contrast, no F or P signals related to ZnF_2 or $Zn_3(PO_4)_2$ was detected in TMP−0 (Supplementary Fig. 22). The XPS analyses provide strong evidences that the TMP−40 electrolyte favors the in-situ formation of gradient interlayer on Zn surface, where ZnF_2 and $Zn_3(PO_4)_2$ dominates the surface layer and inner layer, respectively.

The Kinetic Behavior Of Bivalent Zn On The Electrode/electrolyte Interface

As aforementioned, the SEI with rapid Zn^{2+} transport kinetics and low Zn^{2+} desolvation energy is beneficial for ZMBs to stably work at low temperatures. Thus, we performed temperature-dependent electrochemical impedance spectroscopy (EIS) of Zn||Zn cells at temperature ranging from 20 ^oC to − 30 ^oC in TMP−0 and TMP−40 after 40 cycles (Supplementary Fig. 23), where a dense SEI should be formed in TMP−40. The charge transfer resistance (R_{ct}) and the resistance associated with Zn^{2+} crossing SEI (R_{SEI}) can be extracted from the semicircles in mid-frequency region and the high-frequency region, respectively[24−26]. By Arrhenius-fitting R_{ct} and R_{SEI} over 1000/T, the activation energy of each interface process were obtained, as shown in Fig. 4a, b. Compared with TMP−0, the desolvation energy of Zn^{2+} in the TMP−40 was greatly reduced (70.2 KJ mol^{-1} vs 54.8 KJ mol^{-1}), indicating the outer ZnF_2 facilitate Zn^{2+} desolvation, agreeing with the reported results[36,37]. Moreover, the activation energy for Zn^{2+} transport through the SEI in TMP−40 ($E_{a,SEI}$=52.7 KJ mol^{-1}) is significantly lower than in TMP−0 ($E_{a,SEI}$=64.3 KJ mol^{-1}). This can be well explained by the density functional theory (DFT) calculation results that the $Zn_3(PO_4)_2$ delivers a much smaller migration energy barrier for Zn^{2+} (0.38 eV) (Fig. 4d) and higher affinity with Zn^{2+} (− 1.15 eV) (Fig. 4c) compared with those of ZnF_2 (1.12 eV for Zn^{2+} transport

and weak binding energy of − 0.85 eV with Zn^{2+}). That is, the rich $Zn_3(PO_4)_2$ in the inner SEI serves as the dominant channels for the desolvated Zn^{2+} across the SEI to deposit on the Zn surface, which can facilitate fast Zn^{2+} conduction to mitigate voltage polarization under cold environments[38,39]. Moreover, we prepared SEI containing single ZnF_2 or $Zn_3(PO_4)_2$ to confirm their respective role (Supplementary Fig. 24). Besides, the interface impedance of Zn||Zn cells in the TMP–40 electrolyte can remain stable after 500 cycles, indicating the stable interface due to the formation of ZnF_2–$Zn_3(PO_4)_2$ interlayer (Fig. 4e). In sharp contrast, the TMP–0 electrolyte shows a sharp decrease in the interfacial impedance after 100 cycles, possibly due to the dendrite growth that causes the cell short circuit (Fig. 4f).

In addition, a high mechanical integrity is indispensable for SEI to ensure the long-term cycling and high-capacity plating. To this end, in-situ optical microscopy was performed to observe the morphology evolution at different plating stages. As shown in Fig. 4g, the TMP–40 electrolyte enables the dense deposition without dendrite formation during the whole deposition process and can maintain a smooth surface even at a colossal loading of 50 mAh cm^{-2}. While for the case of TMP–0, uneven spots appear at 10 mAh cm^{-2} and gradually evolve into discontinuous islands as the plating capacity increases, which is consistent with the scanning electron microscopy (SEM) results (Supplementary Fig. 25). The striking contrast in morphology evolution demonstrates that the gradient SEI can effectively suppress the dendrite growth and is highly stable to accommodate the high-loading Zn plating, largely ascribed to the strong bulk modulus of $Zn_3(PO_4)_2$[37]. Taken together, we reasonably conclude that the rich ZnF_2 on the top layer of SEI favors the desolvation of Zn^{2+} and the robust $Zn_3(PO_4)_2$ predominating the inner SEI layer facilitates rapid Zn^{2+} transport. With these admirable characters, it is expected that the as-formed gradient ZnF_2–$Zn_3(PO_4)_2$ SEI can guarantee stable and long-term cycling of Zn metal at low temperatures.

Electrochemical Performance Of Zn Metal Anodes Under Harsh Conditions

It is worth mentioning that these features of the gradient SEI can allow the symmetric Zn cells to stably cycle in the TMP–40 electrolyte at a high current density of 5 mA cm^{-2} at 25 °C and 45 °C (Fig. 5a and Supplementary Fig. 26). In sharp contrast, the cells in TMP–0 quickly failed due to severe Zn dendrite formation and aggravated side reactions. This also manifests that the gradient ZnF_2–$Zn_3(PO_4)_2$ SEI is ultra-stable against the high-temperature and high-rate cycling, underscoring the significance of SEI formation on the interface. Then the galvanostatic cycling stability of Zn metal in the TMP–40 electrolyte was studied at low temperatures with different rates. When the operation temperature was fixed at − 30 °C, the cell in TMP–40 exhibits a stable voltage profile at 2 mA cm^{-2} with an ultralong cycling life up to 3600 hours, which is around 40–fold improvement in cycle life (Fig. 5b). With the superior kinetics in the electrolyte/electrode interface, the TMP–40 electrolyte enables the symmetric cells to operate over long-

term cycles with high rates ranging from 5 mA cm^{-2} to 15 mA cm^{-2} through a transient activation (Supplementary Fig. 27).

Then the cycling temperature was decreased to − 50 °C. Not surprisingly, the cell in TMP–0 cannot work due to the electrolyte solidification (Fig. 5c). While the TMP–40 electrolyte achieves an ultralong lifespan at 0.4 mA cm^{-2} and 0.4 mAh cm^{-2} without obvious fluctuation in overpotential over 6000 hours (~ 8 months). As the discharge depth was increased to 1 mAh cm^{-2}, it is amazing to find that the cell can still maintain an impressive stability without voltage fluctuation over 6000 hours (Supplementary Fig. 28). These observations convectively demonstrate that the as-formed gradient ZnF_2–$Zn_3(PO_4)_2$ SEI with the unique configurations can accelerate the rapid Zn^{2+} desolvation and conduction at low temperatures, which guarantees the ultra-stable cycling with a negligible polarization at rather extreme conditions (low temperatures with high rates). Notably, the Zn||Zn symmetric cells in TMP–40 achieve a rather competitive cumulative capacity over a wide temperature range (Fig. 5d and Supplementary Table 3), far outperforming those of reported low-temperature aqueous Zn metal anodes[8,13,17,19,40,41]. Both top and side views reveal that the surface of Zn electrode after 100 plating/stripping cycles in TMP–40 is highly homogeneous and tightly packed, while the one with TMP–0 exhibits severe cracks (Fig. 5e, f), indicating the gradient SEI layer can effectively suppress the Zn dendrite growth.

The reversibility of Zn plating/stripping was further studied by calculating the Coulombic efficiency (CE) of Zn metal onto titanium (Ti) substrate. At − 30°C with a current density of 1 mA cm^{-2} and a capacity of 0.5 mAh cm^{-2}, the CE in TMP–40 electrolyte quickly increases to 99% within 20 cycles and stabilizes at 99.9% over 3800 cycles along with flat voltage profiles (Fig. 5g and Supplementary Fig. 29). Conversely, the cell with TMP–0 electrolyte exhibits a low CE of around 60% and quickly short circuited at the 9th cycle due to dendrite formation. These contrasts can be maximized at different temperatures ranging from 45°C to − 50°C (Supplementary Fig. 30), well illustrating that the gradient SEI layer is stable against the severe side reaction and maintains superior kinetics at low temperatures.

Electrochemical Performance Of Zn–kvoh Full Cells Under Practical Conditions

To evaluate the practical applications of TMP–40 electrolyte, KVOH was employed as cathode to pair with Zn metal for full cells in the TMP–40 electrolyte due to its superior kinetics (Supplementary Fig. 31). The Zn–KVOH full cell with TMP–40 electrolyte delivers an initial capacity of 329.1 mAh g^{-1} at 5 A g^{-1} and retains a capacity of 323.6 mAh g^{-1} after 2300 cycles at room temperature (Fig. 6a), corresponding to a capacity retention of 98.3%. In contrast, the cell with TMP–0 electrolyte exhibits a slightly higher initial capacity of 344.4 mAh g^{-1} at 5 A g^{-1} possibly due to a higher ionic conductivity, but quickly dropped to 211 mAh g^{-1} after 500 cycles, along with a larger polarization in the charge–discharge voltage profiles (Supplementary Fig. 32). The significant performance improvement is also revealed with high loadings of KVOH (6.37 mg cm^{-2} and 17.6 mg cm^{-2}), at various rates (1 A g^{-1}, 2 A g^{-1} and 10 A g^{-}

^{1}) or even at a higher temperature (45 ^{o}C, 5 A g^{-1}), as shown in Supplementary Figs. 33–35. Impressively, with a high areal loading of KVOH up to 17.6 mg cm^{-2}, the full cell still maintains an areal capacity of 4.37 mAh cm^{-2} after 100 cycles, which meets the requirements of a typical commercial Li-ion battery (4.0 mAh cm^{-2})[42]. In view of the inspiring performance, we further evaluated the application of TMP–40 electrolyte in practical situation by controlling lean electrolyte and low Zn excess. As shown in Fig. 6b, when the KVOH loading increases to 33.75 mg cm^{-2}, the cell still delivers a superhigh initial areal capacity of 9.42 mAh cm^{-1} with lean E/C (6.76 μL mAh^{-1}, the ratio of electrolyte volume to capacity) ratio and low N/P (3.1, the ratio of negative to positive). The corresponding energy density is calculated to be 251.2 Wh kg^{-1} (based on the KVOH mass) with a high capacity retention of 93.3% after 50 cycles. The outstanding performance can be ascribed to the superior kinetics and great robustness of the ZnF_2–$Zn_3(PO_4)_2$ SEI that can allow large amounts of Zn^{2+} to repeatedly strip and plate.

Electrochemical Performance Of Zn–kvoh Full Cells At Low Temperature

By virtue of the favorable SEI formation, the TMP–40 electrolyte can enable the Zn–KVOH full cells to sustain remarkable long lifespan and prominent stability at subzero temperatures. Specifically, when the temperature was decreased to − 30 ^{o}C (Supplementary Fig. 36), the discharge capacity of the cell in the TMP–40 electrolyte remains at 120.6 mAh g^{-1} after 4000 cycles at 1 A g^{-1}, far exceeding that without TMP. Even at a higher rate of 2 A g^{-1} and 5 A g^{-1}, the 40% of TMP addition can prompt the cell to charge/discharge reversibly over 10000 cycles and 1500 cycles, respectively. In stark contrast, the cell with TMP–0 electrolyte failed to work, underscoring the critical role of the gradient SEI formed in the TMP–40 electrolyte. These contrasts are more evident at − 50 ^{o}C, where the cell with TMP–0 cannot provide any capacities due to the electrolyte solidification. Comparatively, the TMP–40 electrolyte can render the full cell to deliver a stable capacity of 50.8 mAh g^{-1} at 0.5 A g^{-1} over 12000 cycles (Fig. 6c). The fluctuations at the 800th, 5000th and 9800th cycle are ascribed to the sudden power outages during the long-term test, which also confirm the good temperature adaptivity of the gradient SEI formed in the TMP–40 electrolyte. Compared with the published works on electrolyte modification for aqueous Zn batteries, this work is undoubtedly prominent in achieving long-cycle stability over a wide temperature range (Fig. 6d, Supplementary Tables 4–5)[4,8,12,14–17,19,22,40,41,43–46]. Post-mortem analyses show that the Zn metal anode after 1000 cycles in the TMP–40 electrolyte can maintain a much flatter and denser surface (Supplementary Fig. 37). The significant performance improvement achieved in the TMP–40 electrolyte at low temperatures strongly validates the gradient SEI with the favorable kinetics can effectively suppress the Zn dendrite growth and ensure the superb cycling behaviors in full cells under extreme conditions.

The exceptional performance of the ZMBs inspired us to further evaluate the low-temperature performance of pouch cell with a size of 4.3 × 5.6 cm in the TMP–40 electrolyte. As shown in Fig. 6e, a reversible capacity of 340.5, 159.4, 122.2 mAh g^{-1} was achieved at 25 ℃ (room temperature), − 30 ℃

and − 50 ℃, respectively. Notably, the pouch cell achieves a superior cycling stability at a low temperature of − 30°C with a high capacity retention of 88.6% after 1200 cycles at 0.25 mA cm^{-2} (Fig. 6f). Even at − 50°C, it can stably cycle for 180 cycles with nearly 100% of capacity retention (Supplementary Fig. 38). Moreover, five series connected pouch cells with a voltage of ~ 5 V can drive an electro-calculagraph normally working for more than 3 min at an extreme temperature of − 50°C (Fig. 6g and Supplementary Fig. 39), further demonstrating its promising potential in the practical applications under harsh conditions.

Discussion

In summary, we have successfully in-situ constructed gradient SEI layer on Zn surface to enable long-cycling and dendrite-free ZMBs at low temperatures by introducing TMP into the aqueous electrolyte. It was found that 40% of TMP addition can regulate the Zn^{2+} solvation sheath and promote the formation of ZnF_2–$Zn_3(PO_4)_2$ gradient SEI, which effectively suppress the parasitic reaction and Zn dendrite growth. Moreover, a combination study of computational and experimental characterizations reveals the outer ZnF_2 can facilitate Zn^{2+} desolvation and the inner $Zn_3(PO_4)_2$ can serve as channels for fast Zn^{2+} conduction, synergistically leading to continuous cycling under cold environments. Remarkably, a record stability was achieved in the symmetric Zn cell at − 50 ^oC with a lifespan of 6000 hours at a relatively high current density of 0.4 mA cm^{-2}. Furthermore, the Zn–KVOH full cell delivers a stable capacity of 50.8 mAh g^{-1} at 0.5 A g^{-1} over 12000 cycles at − 50 ^oC. Full cells with lean electrolyte and low Zn excess also demonstrate the practical feasibility. This work provides a feasible route to achieve highly stable ZMBs under extreme conditions.

Methods

Electrolyte preparation

Zinc trifluoromethanesulfonate ($Zn(OTf)_2$, > 99%) and trimethyl phosphate (TMP, 98%) was purchased from Adamas and Sigma-Aldrich, respectively. A series of electrolytes were formulated by dissolving 2 M $Zn(OTf)_2$ in deionized (DI) water with different volume ratios of TMP from 0%, 5%, 10%, 20%, 40%, 60%, 80–100%. The corresponding electrolyte is marked as TMP–0, TMP–5, TMP–10, TMP–20, TMP–40, TMP–60, TMP–80 and TMP–100, respectively.

Fabrication Of Kvoh Cathode

The synthesis of KVOH was based on a previous method, as reported by Gao[1]. Specifically, 0.364 g of vanadium pentoxide (V_2O_5, 99%, Sigma Aldrich) in 50 ml DI water was mixed with 0.0745 g of potassium chloride (KCl, 99.9%, Sigma Aldrich) in 30 mL DI water, followed by addition of 1.7 mL hydrogen peroxide (H_2O_2, 35%, Fisher Scientific) and 0.5 h of stirring. Then the mixture was transferred into 100 mL Teflon

autoclave and heated at 120°C for 6 h. The green powder was collected by centrifugation, repeated wash with DI water and ethanol, and drying overnight at 60°C.

Preparation Of Znf@zn And Zn(Po)@zn

According to the previous report[2], ZnF_2@Zn was obtained by chemically treating Zn foil with Ammonium fluoride (NH_4F, 99.99%, Aladdin) dispersed in the dimethyl sulfoxide (DMSO, 99.9%, Innochem) solvents. First, 5 mg NH_4F was dispersed in 6 mL DMSO under vigorous stirring for 3 days and then dropped onto the Zn surface, followed by rapidly drying in glove box at 180°C for 10 min. The above operation was repeated 10 times to obtain uniform ZnF_2@Zn. The $Zn_3(PO_4)_2$@Zn was obtained through the chemical reaction between Zn and Diammonium hydrogen phosphate aqueous solution. First, 66 mg Diammonium hydrogen phosphate ($(NH_4)_2HPO_4$, 99.9%, Macklin) was dissolved in 10 mL deionized water to obtain 0.05 M $(NH_4)_2HPO_4$ aqueous solution. Second, Zn plates (φ = 12 mm) were immersed into the above solution under stirring for 5 h, followed by repeated washing and drying at 80°C for standby.

Material Characterizations

Differential scanning calorimetry (DSC, METTLER TOLEDO DSC3) was used to measure the freezing point of the hybrid electrolyte at a temperature range from − 150 ^{o}C to 25 ^{o}C, which was carried out in a liquid nitrogen cooling system with a heating rate of 5°C min^{-1}. Fourier Transform Infrared (FT-IR) analysis was conducted on Nicolet iS50. Raman spectroscopy was recorded on LabRAM HR Evolution with an excitation wavelength of 633 nm. The changes of hydrogen bonds were analyzed by nuclear magnetic resonance (NMR, AVANCE III 400MHz) with deuterated DMSO. Scanning electron microscopy (SEM) images were collected using FEI Microscope (JSM-7900F). Transmission electron microscopy (TEM) and energy dispersive X-ray spectroscopy (EDS) were performed on Talos F200X G2. X-ray diffraction (XRD) measurements were obtained on diffractometer (Smart Lab 9 KW) with a Cu-target X-ray tube (λ = 0.154 nm) at 150 mA and 40 kV. The compositions of solid electrolyte interphase (SEI) were determined by X-ray photoelectron spectroscopy (XPS, Axis Ultra DLD) using monochromatic 1486.7 X-ray source.

Electrode Preparation

For the coin cell, the as-prepared KVOH was mixed with super P carbon black (SUPER P, TIMCAL) and polyvinyldifluoride (PVDF, Sinopharm) based on a weight ratio of 7:2:1 (routine test) or 8:1:1 (high loading test), which was dispersed in N-methyl-2-pyrrolidinone (NMP, Sinopharm) to form a slurry. Then the slurry was casted onto carbon paper disks with a diameter of 10 mm and dried overnight at 60°C in a vacuum oven. The preparation procedures of KVOH cathode for punch cells were similar to the above description, except the electrode size is 4.3 × 5.6 cm.

Electrochemical Measurements

2032-type coin cells were assembled to measure the Coulombic efficiency and cycling stability of Zn metal anode (100 μm) on standard battery tester (LAND-CT2001A) at different temperatures controlled by cryostat (− 50 ^{o}C), fridge (− 30 ^{o}C) and oven (25 ^{o}C, 45 ^{o}C). The separator used was glass fiber (90 μm in thickness, Waterman GF/D). The cycling stability was evaluated in symmetric cells composed of two identical Zn disks in the electrolyte of TMP–0 and TMP–40 at different current densities and capacities. For the measurement of Coulombic efficiency, the coin cells were composed of a titanium (Ti) foil as working electrode (substrate for Zn plating and stripping), and a piece of Zn foil as counter and reference electrode. A constant current with a constant capacity (the amount of Zn deposited) was applied to the electrode, followed by Zn stripping via charging to 1 V (versus Zn/Zn^{2+}). The Coulombic efficiency of each cycle was calculated as the amount of Zn stripped (based on capacity extracted) divided by the amount of Zn plated (based on capacity deposited) onto the Ti foil. Linear sweep voltammetry (LSV) of the hybrid electrolytes was measured using Ti||Zn asymmetric at a scan rate of 5 mV s^{-1} in a voltage range of − 0.5 ~ 3 V (versus Zn/Zn^{2+}) on an electrochemical workstation (Ivium-n-Stat, Nederlanden).

The ionic conductivity of hybrid electrolytes at different temperatures was measured by EIS via symmetrical cells consisted of two parallel Pt-plate electrodes (10 mm×10 mm). The distance between two electrodes is 10 mm and the applied frequency range was from 10^{5} Hz to 10^{-1} Hz with 5 mV AC amplitude. The ionic conductivity of hybrid electrolyte was calculated by the following equation:

$$\sigma = \frac{L}{R_s \times A} \quad (1)$$

Where σ is the ionic conductivity of the electrolyte (S cm^{-1}), R_s is the electrolyte resistance (Ω), which corresponds to the intercept of Nyquist plot. L (cm) is the distance between two Pt-plate electrodes. A (cm^2) stands for the area of Pt electrode.

The electrochemical performance of Zn–KVOH full cell was evaluated by using both 2032-type coin-cell and pouch-cell. For the routine test of coin-type full cell, the typical mass loading of active materials (KVOH) is around 1.2 ~ 1.5 mg cm^{-2}, glass fiber (GF/D, 90 μm in thickness) as separator and 100 μm Zn metal as anode. The electrolyte was fixed to around 130 μL. The galvanostatic discharge/charge tests were performed using LAND-CT2001A instruments in a voltage range of 0.2–1.6 V (vs Zn/Zn^{2+}). Electrochemical impedance spectroscopy (EIS) measurements were carried out on an electrochemical workstation (Ivium-n-Stat, Nederlanden) from 10^{5} Hz to 10^{-2} Hz, and the perturbation amplitude was 5 mV. All the tests at different temperatures were carried out after 2 hours of resting.

For the test of coin-type full cell with high-loading cathode (33.75 mg cm^{-2}), we used carbon cloth as current collector, thin glass fiber (GF/A, 55 μm in thickness) as separator, 50 μm Zn metal as anode and the lean electrolyte (50 μL) is dropped on the cathode side.

Computational Details

Molecular dynamics simulations

In this work, the solvation environment of TMP–0 (molar ratio, $Zn(OTf)_2$:H_2O = 1:27.79) and TMP–40 (molar ratio, $Zn(OTf)_2$:TMP:H_2O = 1:1.74:16.67) were simulated. The TMP–0 model system involves 70 $Zn(OTf)_2$ salt molecules and 1945 H_2O molecules, while the TMP–40 one contains 70 $Zn(OTf)_2$ salt molecules, 122 TMP molecules, and 1167 H_2O molecules. Packmol[3] was used to build initial configuration of the two model systems. LAMMPS[4] was used to perform the molecular simulations. All atom molecular dynamics simulations were carried out using PCFF-INTERFACE force field[5]. Constant NVT conditions are enforced using a Nosé-Hoover thermostat with a relaxation time of 100 fs and a temperature of 300 K[6]. The density of each electrolyte solution was determined from 500 ps molecular dynamics simulation in the NPT ensemble at the same thermodynamic conditions. Equations of motions were integrated using the velocity–Verlet method with a 1.0 fs time step. The cut-offs for all the non-bonded interactions are 12 Å. All results reported here are statistical averages taken from runs of 1000 ps in length, each preceded by 1500 ps of equilibration. The atomic coordinates were collected every 1.0 ps for statistical analysis.

Quantum Chemistry Calculations

For the relative binding energy of Zn^{2+} with different species, the structures were fully optimized by using the B3LYP[7,8] method in the level of 6–31 + + G (d, p) basis set. Analytical vibrational frequency was calculated at the same level. The Zn^{2+} cation carries two unit of positive charge. The interaction energy was calculated as following:

$$\Delta E_{inter} = E_{total} - (E_{Zn} + E_{solvent}) \quad (2)$$

ΔE_{inter} represents the interaction energy, E_{total}, E_{zn} and $E_{solvent}$ are the energies of the complex, Zn^{2+} cation, and solvent (H_2O or TMP), respectively. The more negative the magnitude of interaction energy, the more favorable the interaction between the Zn^{2+} cation and the solvent is. All calculations were performed with the Gaussian 09 program.

For the migration energy barrier of zinc ions between different components, we have employed the Vienna Ab initio Simulation Package (VASP) to perform all density functional theory (DFT) calculations within spin-polarized frame[9,10]. The elemental core and valence electrons were represented by the projector augmented wave (PAW) method and plane–wave basis functions with a cutoff energy of 400 eV. Generalized gradient approximation with the Perdew-Burke-Ernzerhof (GGA-PBE) exchange-correlation functional was employed in all the calculations[11,12]. Geometry optimizations were performed with the force convergency smaller than 0.05 eV/Å, where the same convergency were applied for the locating of

transition states through the constrained optimizations (NEB). The atoms at bottom of $Zn_3(PO_4)_2$ (− 121) surfaces (43 atoms) and the ZnF_2 (111) surfaces (44 atoms) were fixed in all the calculations. Monkhorst-Pack k-points of 3×2×1 and 2×2×1 were applied for all the surface calculations for $Zn_3(PO_4)_2$ (− 121), and ZnF_2 (111), respectively. To obtain transition states, the bulk structures of $Zn_3(PO_4)_2$ and ZnF_2 (111) have been optimized with the Monkhorst-Pack k-point of 3×3×3 and 5×3×8, respectively.

Declarations

Acknowledgements

This work was supported by the Ministry of Science and Technology of China (2021YFA1201900), National Natural Science Foundation of China (No. 22105107) and Fundamental Research Funds for the Central Universities (No. 020/C029201005). We thank the Haihe Laboratory of Sustainable Chemical Transformations for financial support. H.W. acknowledge the Young Elite Scientists Sponsorship Program by Tianjin.

Author contributions

H.W. and W.W. conceived the original idea. W. W., F. W. and H. W. designed all the experiments. W. W., S. C., X. L. and J. C. carried out the experiments. W. W., S. C., X. L., R. H., Y. W., F. W. and H. W. analyzed the experimental data. W. W., F. W. and H. W. co-wrote the paper. All authors were involved in discussion of the experimental results and preparing of the manuscript.

Competing interests

The authors declare no competing interests.

References

1. Wang, F. et al. Highly reversible zinc metal anode for aqueous batteries. Nat. Mater. **17**, 543–549 (2018).
2. Xie, C. L. et al. Issues and solutions toward zinc anode in aqueous zinc-ion batteries: A mini review. Carbon Energy **2**, 540–560 (2020).
3. Zhang, Y. M., Howe, J. D., Ben-Yoseph, S., Wu, Y. T. & Liu, N. Unveiling the origin of alloy-seeded and nondendritic growth of Zn for rechargeable aqueous Zn batteries. ACS Energy Lett. **6**, 404–412 (2021).
4. Han, D. L. et al. A non-flammable hydrous organic electrolyte for sustainable zinc batteries. Nat. Sustain. **5**, 205–213 (2022).
5. Li, C., Jin, S., Archer, L. A. & Nazar, L. F. Toward practical aqueous zinc-ion batteries for electrochemical energy storage. Joule **6**, 1727–1742 (2022).

6. Wu, H. Ice as solid electrolyte to conduct various kinds of ions. Angew. Chem. Int. Ed. **58**, 12569–12573 (2019).
7. Zhang, Q. et al. Modulating electrolyte structure for ultralow temperature aqueous zinc batteries. Nat. Common. **11**, 4463 (2020).
8. Chang, N. N. et al. An aqueous hybrid electrolyte for low-temperature zinc-based energy storage devices. Energy Environ. Sci. **13**, 3527–3535 (2020).
9. Feng, Y. et al. Challenges and advances in wide-temperature rechargeable lithium batteries. Energy Environ. Sci. **15**, 1711–1759 (2022).
10. Matsumoto, M., Saito, S. & Ohmine, I. Molecular dynamics simulation of the ice nucleation and growth process leading to water freezing. Nature **416**, 409–413 (2002).
11. Moore, E. B. & Molinero, V. Structural transformation in supercooled water controls the crystallization rate of ice. Nature **479**, 506–508 (2011).
12. Cao, L. S. et al. Highly reversible aqueous zinc batteries enabled by zincophilic–zincophobic interfacial layers and interrupted hydrogen-bond electrolytes. Angew. Chem. Int. Ed. **60**, 18845–18851 (2021).
13. Sun, T. J. et al. An ultralow-temperature aqueous zinc-ion battery. J. Mater. Chem. A **9**, 7042–7047 (2021).
14. Gao, S. Y. et al. High energy and stable subfreezing aqueous Zn-MnO_2 batteries with selective and pseudocapacitive Zn-ion insertion in MnO_2. Adv. Mater. **34**, 2201510 (2022).
15. Cao, L. S. et al. Solvation structure design for aqueous Zn metal batteries. J. Am. Chem. Soc. **142**, 21404–21409 (2020).
16. Hao, J. N. et al. Boosting zinc electrode reversibility in aqueous electrolytes by using low-cost antisolvents. Angew. Chem. Int. Ed. **60**, 7366–7375 (2021).
17. Wang, J. W. et al. Low-temperature and high-rate Zn metal batteries enabled by mitigating Zn^{2+} concentration polarization. Chem. Eng. J. **433**, 134589 (2022).
18. Ming, F. W. et al. Co-solvent electrolyte engineering for stable anode-free zinc metal batteries. J. Am. Chem. Soc. **144**, 7160–7170 (2022).
19. Huang, S. W. et al. Antifreezing hydrogel electrolyte with ternary hydrogen bonding for high-performance zinc-ion batteries. Adv. Mater. **34**, 2110140 (2022).
20. Lu, H. Y. et al. Multi-component crosslinked hydrogel electrolyte toward dendrite-free aqueous Zn ion batteries with high temperature adaptability. Adv. Funct. Mater. **32**, 2112540 (2022).
21. Yang, Q. et al. Stabilizing interface pH by N-modified graphdiyne for dendrite-free and high-rate aqueous Zn-ion batteries. Angew. Chem. Int. Ed. **61**, e202112304 (2021).
22. Han, D. L. et al. A self-regulated interface toward highly reversible aqueous zinc batteries. Adv. Energy Mater. **12**, 2102982 (2022).
23. Zampardi, G. & La Mantia, F. Open challenges and good experimental practices in the research field of aqueous Zn-ion batteries. Nat. Commun. **13**, 687 (2022).

24. Yao, Y. X. et al. Regulating interfacial chemistry in lithium-ion batteries by a weakly solvating electrolyte. Angew. Chem. Int. Ed. **60**, 4090–4097 (2021).
25. Wang, X. S. et al. Hybrid electrolyte with dual-anion-aggregated solvation sheath for stabilizing high-voltage lithium-metal batteries. Adv. Mater. **33**, 2007945 (2021).
26. Zhang, N. et al. Critical review on low-temperature Li-ion/metal batteries. Adv. Mater. **34**, 2107899 (2022).
27. Wang, J. H. et al. Fire-extinguishing organic electrolytes for safe batteries. Nat. Energy **3**, 22–29 (2018).
28. Naveed, A. et al. A highly reversible Zn anode with intrinsically safe organic electrolyte for long-cycle-life batteries. Adv. Mater. **31**, 1900668 (2019).
29. Zhang, S. C., Li, S. Y. & Lu, Y. Y. Designing safer lithium-based batteries with nonflammable electrolytes: A review. eScience **1**, 163–177 (2021).
30. Okazaki, Y., Taniuchi, T., Mogami, G., Matubayasi, N. & Suzuki, M. Comparative study on the properties of hydration water of Na- and K-halide ions by Raman OH/OD-stretching spectroscopy and dielectric relaxation data. J. Phys. Chem. A **118**, 2922–2930 (2014).
31. Dong, Y. et al. Non-concentrated aqueous electrolytes with organic solvent additives for stable zinc batteries. Chem. Sci. **12**, 5843–5852 (2021).
32. Suo, L. M. et al. “Water-in-salt” electrolyte makes aqueous sodium-ion battery safe, green, and long-lasting. Adv. Energy Mater. **7**, 1701189 (2017).
33. Chen, Z. et al. Anion solvation reconfiguration enables high-voltage carbonate electrolytes for stable Zn/graphite cells. Angew. Chem. Int. Ed. **59**, 21769–21777 (2020).
34. Nakagawa, H. et al. Electrochemical Raman study of plane graphite negative-electrodes in electrolytes containing trialkyl phosphoric ester. J. Power Sources **212**, 148–153 (2012).
35. Wang, L. L. et al. Ultralong cycle stability of aqueous zinc-ion batteries with zinc vanadium oxide cathodes. Sci. Adv. **5**, eaax4279 (2019).
36. Wang, D. D. et al. Site-selective adsorption on ZnF_2/Ag coated Zn for advanced aqueous zinc-metal batteries at low temperature. Nano Lett. **22**, 1750–1758 (2022).
37. Chu, Y. Z. et al. In situ built interphase with high interface energy and fast kinetics for high performance Zn metal anodes. Energy Environ. Sci. **14**, 3609–3620 (2021).
38. Cao, L. S., Li, D., Deng, T., Li, Q. & Wang, C. S. Hydrophobic organic-electrolyte-protected zinc anodes for aqueous zinc batteries. Angew. Chem. Int. Ed. **59**, 19292–19296 (2020).
39. Zeng, X. H. et al. Electrolyte design for in situ construction of highly Zn^{2+}-conductive solid electrolyte interphase to enable high-performance aqueous Zn-ion batteries under practical conditions. Adv, Mater. **33**, 2007416 (2021).
40. Hou, Z., Lu, Z. H., Chen, Q. W. & Zhang, B. Realizing wide-temperature Zn metal anodes through concurrent interface stability regulation and solvation structure modulation. Energy Storage Mater. **42**, 517–525 (2021).

41. Zhou, J. et al. Highly Reversible and Stable Zn Metal Anode under Wide Temperature Conditions Enabled by Modulating Electrolyte Chemistry. Chem. Eng. J. **442**, 136218 (2022).
42. Zhang, L. et al. Enhanced polysulfide regulation via porous catalytic V_2O_3/V_8C_7 heterostructures derived from metal – organic frameworks toward high-performance Li – S batteries. ACS Nano **14**, 8495–8507 (2020).
43. Du, H. H. et al. Improving zinc anode reversibility by hydrogen bond in hybrid aqueous electrolyte Chem. Eng. J. **427**, 131705 (2022).
44. Sun, P. et al. Simultaneous Regulation on Solvation Shell and Electrode Interface for Dendrite-free Zn ion batteries achieved by a low-cost glucose additive. Angew. Chem. Int. Ed. **60**, 18247–18255 (2021).
45. Yang, G. S. et al. An aqueous zinc-ion battery working at – 50°C enabled by low-concentration perchlorate-based chaotropic salt electrolyte. Ecomat **4**, e12165 (2022).
46. Liu, D. S. et al. Regulating the electrolyte solvation structure enables ultralong lifespan Vanadium-based cathodes with excellent low-temperature Performance. Adv. Funct. Mater. **32**, 2111714 (2022).

Figures

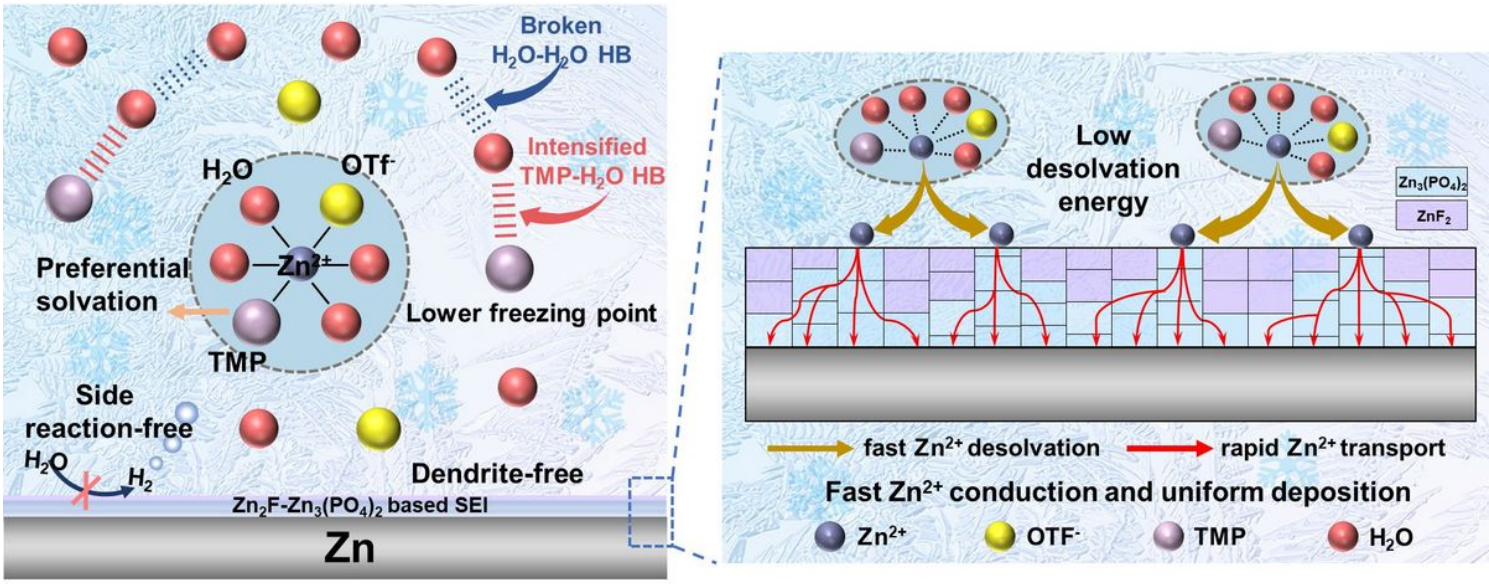

Figure 1

Schematic illustration of ZnF_2-$Zn_3(PO_4)_2$ interlayer formed in the hybrid electrolyte to facilitate the Zn^{2+} desolvation and conduction across the SEI for dendrite-free Zn deposition at subzero temperatures.

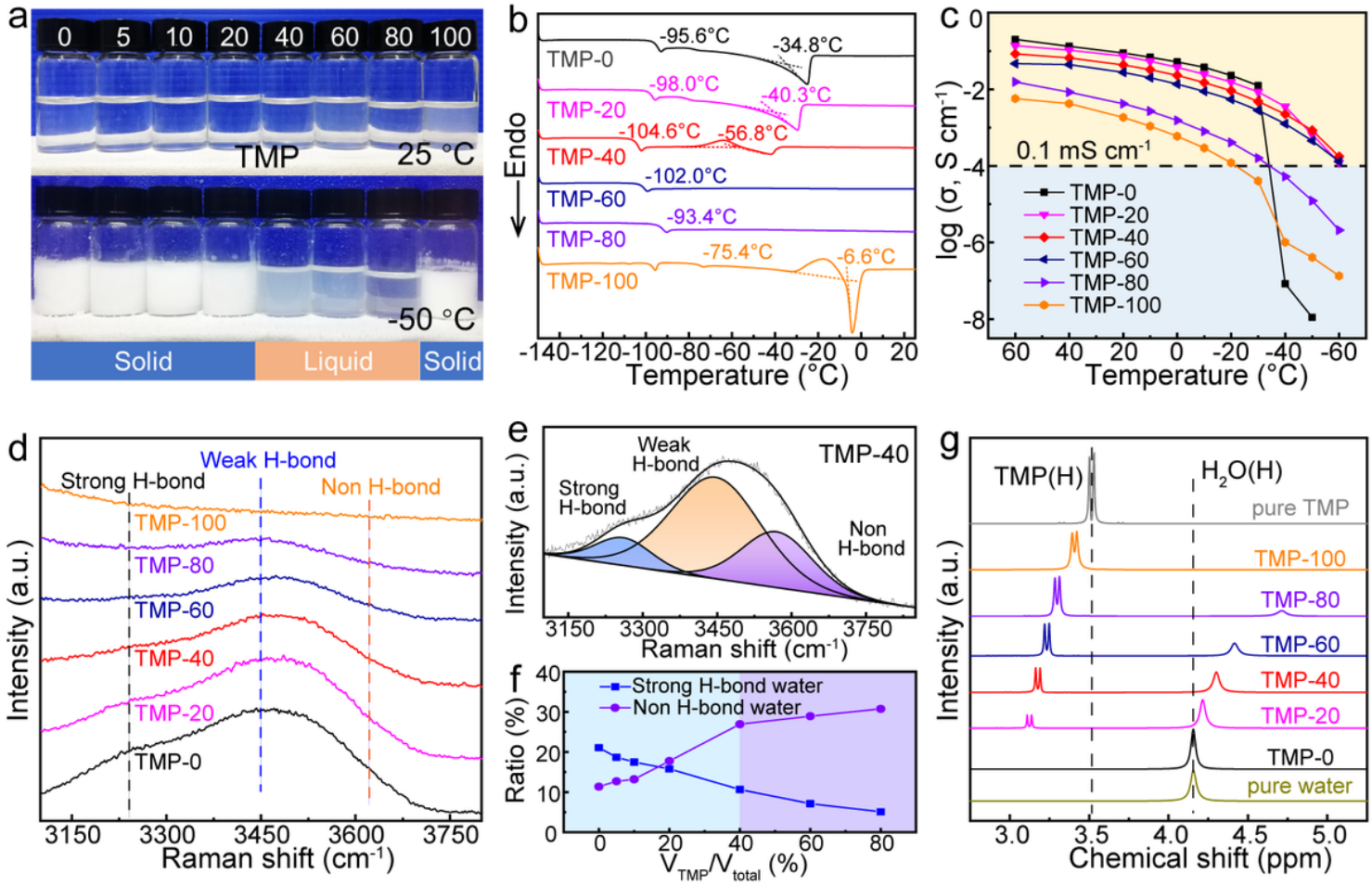

Figure 2

Characterizations of the TMP/water hybrid electrolytes with different TMP contents to explore the optimal formulation for low-temperature ZMBs. a The photographs of hybrid electrolytes at 25 °C (top) and −50 °C (bottom). **b** DSC curves to obtain the freezing points. **c** Ionic conductivities at different temperatures. **d** The Raman spectra of O–H stretching vibration. **e** The fitted O–H stretching vibration of TMP–40 electrolyte. **f** Ratios of strong H-bond and non H-bond water with TMP content in the hybrid electrolyte. **g** ^{1}H chemical shift of water with different TMP contents.

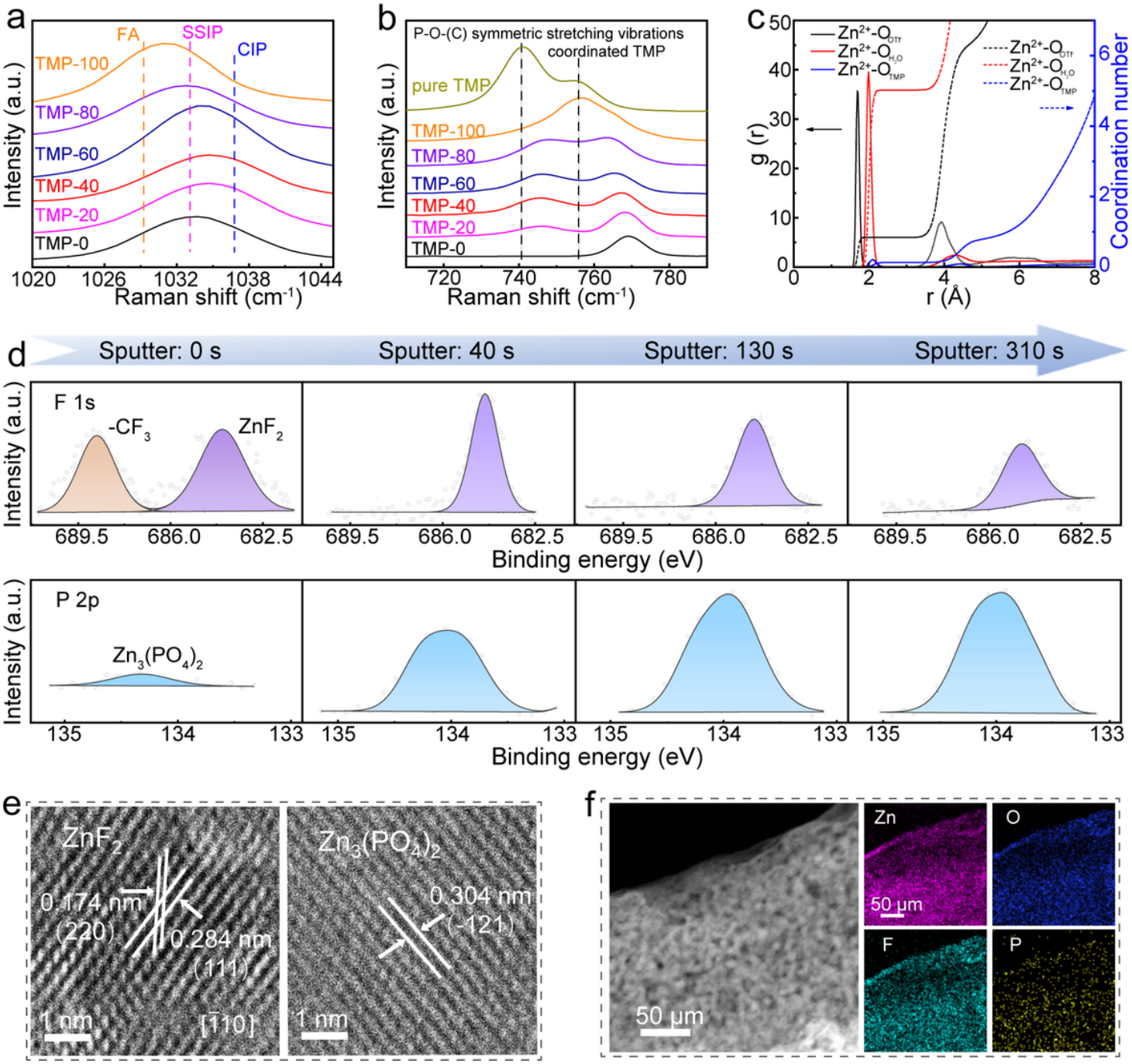

Figure 3

Characterizations of Zn^{2+} solvation structure and the in-situ SEI components. a SO_3 stretching mode in Raman spectra for different hybrid electrolytes. **b** The P–O–(C) symmetric stretching vibration of different hybrid electrolytes. **c** Profiles of radial distribution function g(r) (solid line) and its integral that represents the coordination number (dash-dotted line) of Zn^{2+} with O in different components of TMP–40 electrolyte. **d** XPS F 1s and P 2p spectra with increasing sputtering time. **e** HRTEM images of Zn surface after cycling by Zn||Zn symmetric cells with TMP–40 electrolyte. **f** Element distribution of SEI formed on the Zn surface in TMP–40 electrolyte.

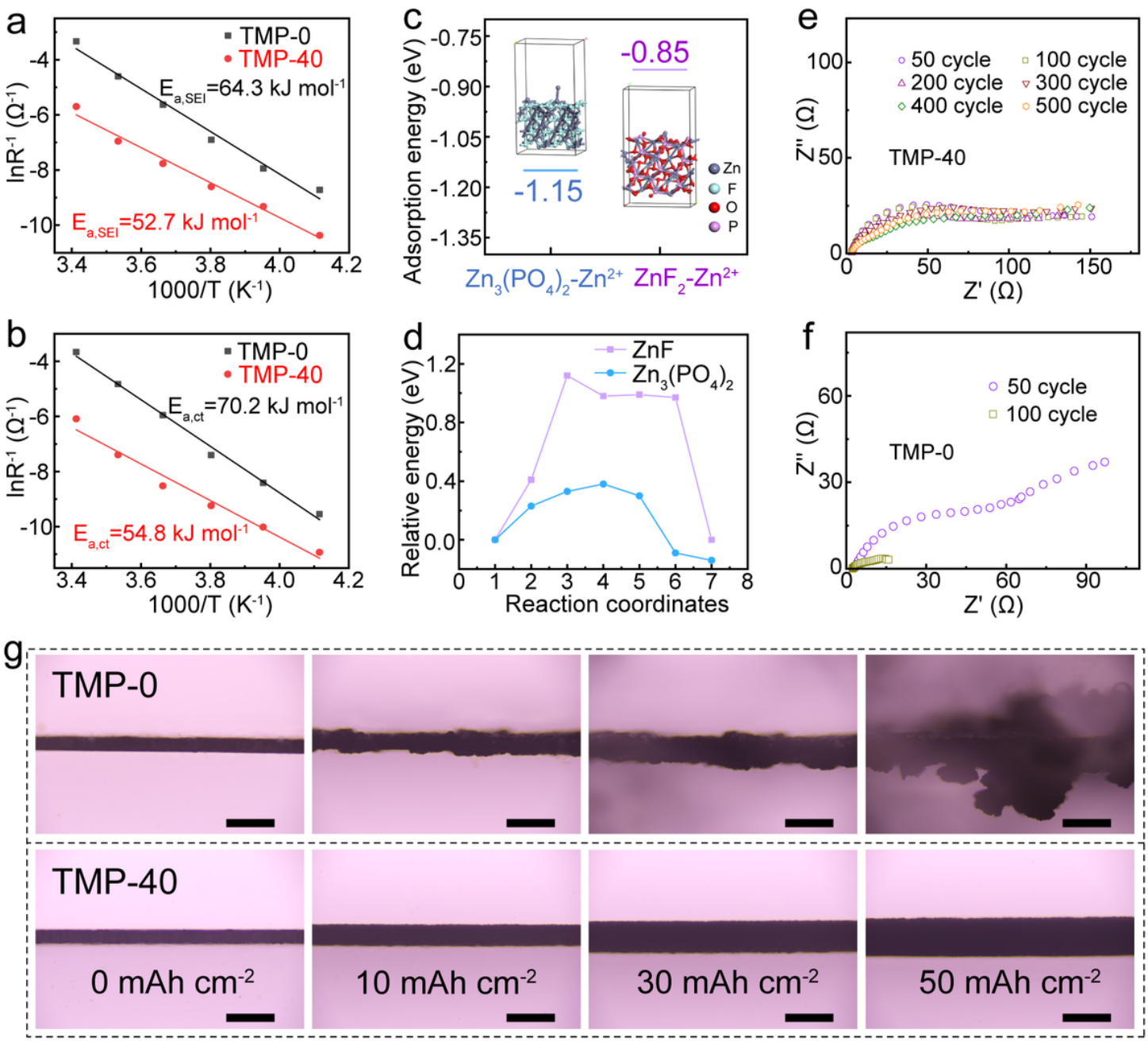

Figure 4

Property and function study of SEI in-situ formed on Zn surface in the electrolyte of TMP−40. Arrhenius curves and the activation energies of **a** R_{SEI} and **b** R_{ct} derived from the Nyquist plots of Zn||Zn cells with TMP−0 or TMP−40 electrolyte after 40 cycles. **c** Adsorption energy of Zn^{2+} with ZnF_2 and $Zn_3(PO_4)_2$. **d** Migration energy barrier of Zn^{2+} across ZnF_2 and $Zn_3(PO_4)_2$ interlayer. Electrochemical impedance spectra of Zn||Zn symmetric cells in **e** TMP−40 electrolyte and **f** TMP−0 electrolyte after different cycles. **g** In-situ optical observation of Zn deposition process in the electrolyte of TMP−0 (top) and TMP−40 (bottom). The scale bar is 200 μm.

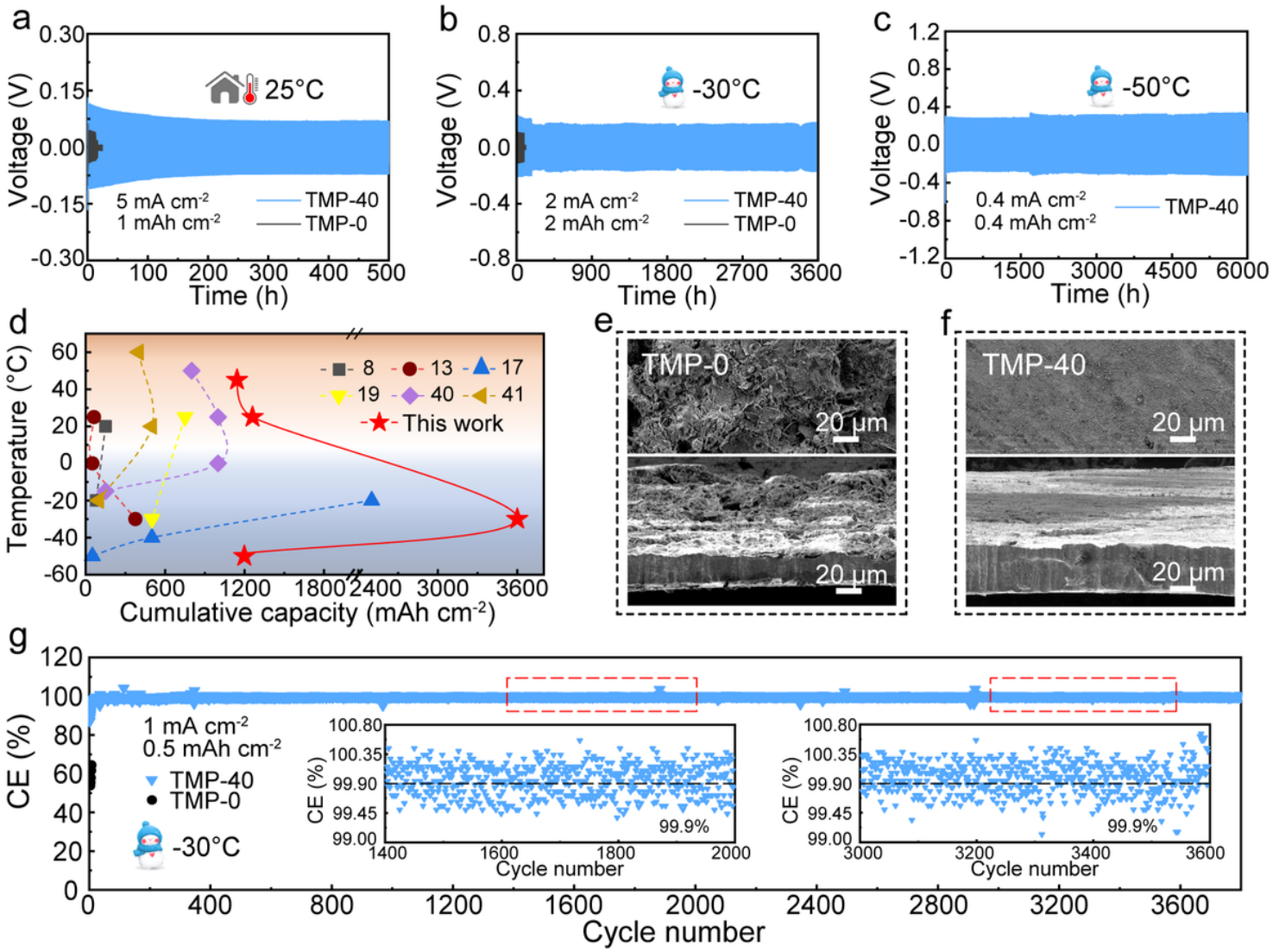

Figure 5

Galvanostatic cycling stability of symmetrical Zn cells with TMP–40 and TMP–0 electrolytes, respectively, at a temperature of **a** 25 °C, **b** −30 °C and **c** −50 °C. **d** Comparison of the cumulative capacity at wide temperatures in our work with other reported results. Top-view (top) and cross-section (bottom) SEM images of symmetric Zn cells after 100 cycles with electrolytes of **e** TMP–0 and **f** TMP–40. **g** Long-term Zn plating/stripping CE in TMP–40 and TMP–0 electrolytes at −30 °C. Insets: the magnified views of selected cycles.

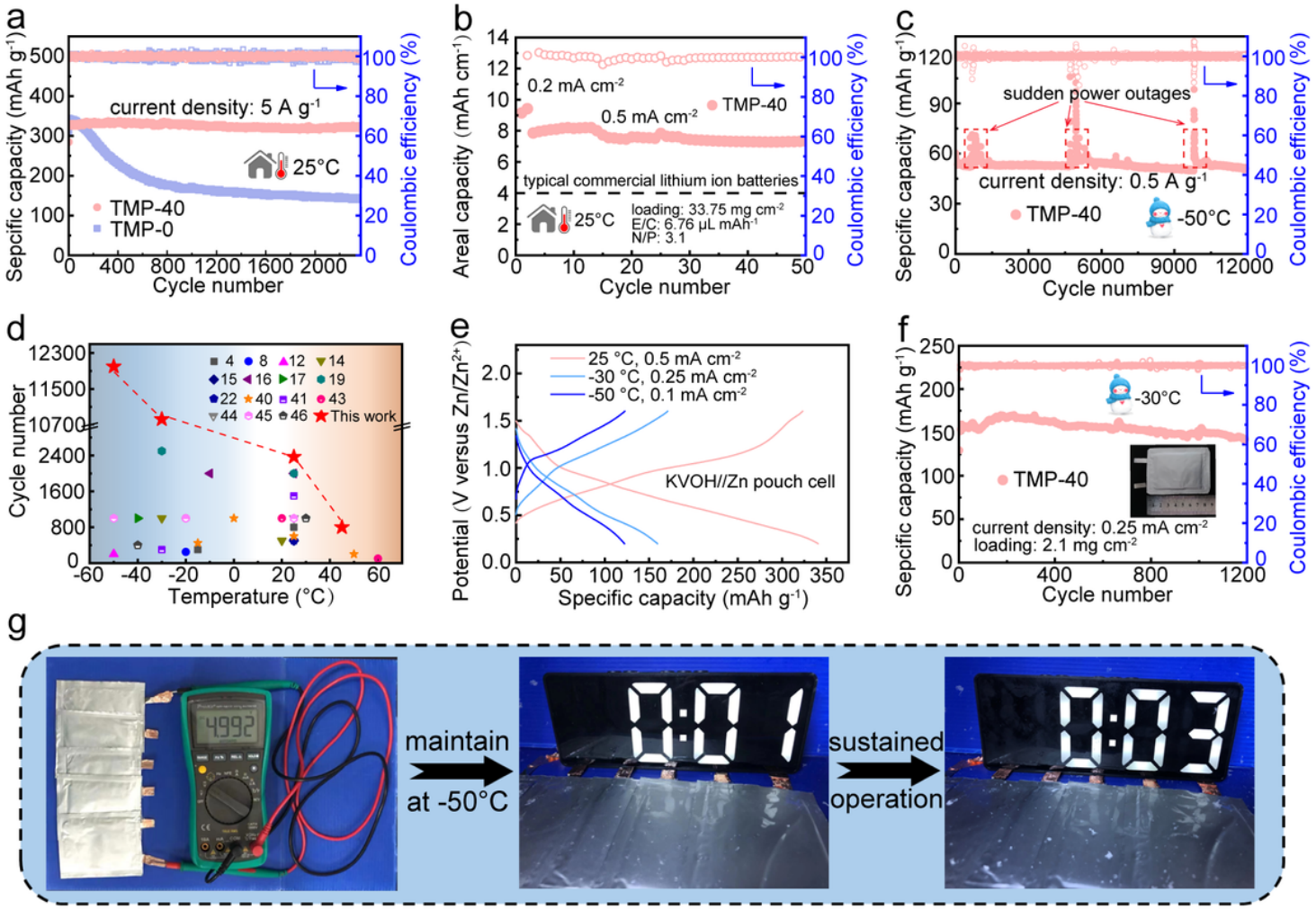

Figure 6

Electrochemical performance of Zn–KVOHfull cells. a Cycling performance of Zn–KVOH cells in the electrolyte of TMP–0 and TMP–40 at 25 °C. **b**Zn–KVOH full cell test under practical conditions with TMP–40 electrolyte. **c** Cycling performance of Zn–KVOH cells with TMP–40 electrolyte at −50 °C. **d** Comparison of the cycling performance of full cells at wide temperatures achieved in this work with those reported ones in literatures. **e** Discharge–charge curves of Zn–KVOH pouch cell with TMP–40 electrolyte at 25 °C, −30 °C and −50 °C. **f** Cycling performance of pouch cell with TMP–40 electrolyte at −30 °C. **g** Pictures of the five series connected pouch cells to drive the calculagraph working for more than 3 min at −50 °C.

Supplementary Files

This is a list of supplementary files associated with this preprint. Click to download.

- SupportingInformation.docx